Numerical Simulation and Chaos Characterization of a Double Pendulum with Magnetic Damping

Ankush Chakrabarty[1] and Dr. Parimal Sarkar[1]

[1]Department of Physics, Coochbehar College, Coochbehar 736101, India.

Submitted on 03-09-2025
Accepted on 13-04-2026

Abstract

This paper investigates the nonlinear dynamics of a planar double pendulum subjected to a magnetic (eddy-current-type) damping torque acting on each bob. Starting from the Lagrangian, we derive the coupled equations of motion including the damping torques, reduce them to an explicit closed-form first-order system, and integrate them numerically with a fourth-order Runge–Kutta scheme across three damping strengths ($k_m = 0$, 0.05, and 0.3 N·m·s). Time series, phase portraits, Poincaré sections, energy decay, and finite-time maximal Lyapunov exponent estimates are used together, rather than in isolation, to characterize the qualitative transition from chaotic to regular dynamics as damping increases. We report this transition cautiously: the finite-time Lyapunov estimate at $k_m = 0$ is slightly negative even though the corresponding Poincaré section and phase portraits are visibly chaotic, a known artefact of short integration windows in weakly chaotic systems, and we treat the multi-diagnostic qualitative trend — not any single numerical exponent — as the reliable result. We connect the phenomenological damping coefficient to eddy-current material parameters, explicitly discuss the mathematical equivalence of the present linear damping law to viscous damping and its limits of validity, validate the integrator against energy-conservation and time-step-convergence checks, and outline the scope, limitations, and pedagogical value of the study.

Keywords: Double pendulum, Magnetic (eddy-current) damping, Deterministic chaos, Lyapunov exponent, Poincaré section, Lagrangian mechanics, Nonlinear dynamics education.

Symbol	Meaning
θ_1, θ_2	Angular displacement of bob 1, bob 2 from the vertical
ω_1, ω_2	Angular velocity, $\omega_i \equiv \dot{\theta}_i$
m_1, m_2	Bob masses
L_1, L_2	Pendulum arm lengths
g	Gravitational acceleration
k_m	Magnetic (eddy-current) damping coefficient (assumed equal at both joints)
$\tau_{d,i}$	Damping torque at joint i
$\mathcal{L}, F$	Lagrangian; Rayleigh dissipation function
σ, B, t, A, r	Conductivity, field strength, plate thickness, area, radius (Section 3.2)
γ	Nondimensional damping ratio
M, C, K	Mass, damping, and stiffness matrices of the linearized system (Section 3.5)
Ω_1, Ω_2	Small-oscillation normal-mode frequencies of the linearized system (Section 3.5)
s	Complex growth rate of a linearized normal mode, $\boldsymbol{\theta} \propto e^{st}$ (Section 3.5)
λ	Maximal Lyapunov exponent (Sections 3.6, 6)
T	Total simulated physical time (40 s throughout)
Δt	Integration time step

1 Introduction

The double pendulum is a prototypical system in nonlinear dynamics, displaying behaviours ranging from simple periodic motion to fully developed chaos. Its extreme sensitivity to initial conditions makes it a natural testbed for studying deterministic chaos, both in research and in the classroom.

Dissipation in real systems can arise from viscous drag, mechanical friction, or electromagnetic effects such as eddy-current (magnetic) damping. Magnetic damping is attractive in precision mechanical systems because it is contactless and wear-free, and it can be tuned via magnetic field strength or conductor geometry. This tunability, rather than any exotic mathematical form, is the practical motivation for studying it here.

This paper presents a theoretical derivation and numerical exploration of a double pendulum incorporating magnetic damping, with two aims. First, at the research level, we quantify how the strength of a contactless damping torque reshapes the phase space of a two-degree-of-freedom nonlinear system, using explicit equations of motion together with several complementary chaos diagnostics. Second, at the pedagogical level, we frame the study so that it is directly reproducible in a computational-physics laboratory, with explicit learning outcomes.

We emphasize at the outset — and return to in Section 3.3 — that the damping law adopted here is the standard linear, low-velocity model of eddy-current damping, and that in this regime it is mathematically identical in form to linear viscous damping. The distinguishing physical content of the study is therefore not a new equation of motion in the abstract sense, but the specific combination of a physically motivated, contactless damping mechanism with a systematic, multi-diagnostic chaos characterization of the two-body system, discussed next.

2 Literature Review

Foundational treatments of nonlinear dynamics and chaos, such as those by Strogatz [1] and Moon [2], provide the theoretical backdrop for the present study. Early numerical and experimental investigations of the double pendulum established its chaotic character and sensitivity to initial conditions [3, 4]; Levien and Tan [4] in particular built a physical apparatus and compared measured Poincaré sections against simulation, which is the kind of experimental benchmark that the present, purely numerical study still lacks (see Section 7.3). Stachowiak and Okada [5] carried out a systematic numerical study of the undamped double pendulum using bifurcation diagrams and Lyapunov exponents computed across a range of energies, rather than at isolated parameter values, illustrating the value of a dense parameter sweep — a methodological point we adopt as an explicit item for future work (Section 7.3).

Magnetic (eddy-current) damping has a separate history in single-degree-of-freedom systems, where it is shown to provide smooth, contactless dissipation [6], and it remains an active area of applied research: Polczyński et al. [7] designed and characterized a large-scale eddy-current damper for structural vibration control, and Khomeriki [8] analysed parametric-resonance-induced chaos in a magnetically damped driven pendulum, showing that magnetic dissipation can both suppress and, under parametric forcing, induce chaotic transitions.

More recent work on the double pendulum specifically has emphasized quantitative chaos diagnostics. Hillebrand et al. [9] used Lagrangian descriptors to map the regular and chaotic regions of the double-pendulum phase space, while Cabrera et al. [10] quantified the fraction of phase space occupied by chaotic versus regular motion as a function of energy. Both studies, however, consider the idealized (undamped) double pendulum over a fine energy grid; neither incorporates a physically motivated dissipation mechanism. Conversely, the magnetic-damping studies above are confined to single-degree-of-freedom systems. Literature that combines the two — magnetic damping in a coupled, two-degree-of-freedom chaotic system — remains sparse.

2.1 Positioning Relative to Prior Work

Rather than asserting priority claims outright, we position the present study relative to the specific papers discussed above, and note explicitly where our evidence for a gap is necessarily limited to the literature we have reviewed.

Damped Lagrangian model. The papers on magnetic damping cited above [6, 8, 7] address single pendula or engineering dampers; the double-pendulum chaos papers [3, 5, 9, 10] consider the undamped or viscously damped case. We are not aware of a published closed-form Lagrangian derivation of the double pendulum with an eddy-current-type damping torque at both joints; Section 3.1 provides one.

Coefficient-to-physics link. Existing eddy-current pendulum studies estimate k_m for a single body. Section 3.2 extends the same scaling argument to the two-body case. This is a modest, incremental extension of established eddy-current theory [6, 7] rather than a new physical result.

Multi-diagnostic damping sweep. To our knowledge, no published study reports time series, phase portraits, Poincaré sections, energy decay, and Lyapunov estimates together across a damping sweep for this specific system; prior double-pendulum chaos papers apply a subset of these diagnostics to the undamped case only, and prior magnetic-damping papers report energy or amplitude decay without Poincaré or Lyapunov analysis. We present this combination in Section 5.4, while acknowledging in Section 7.3 that our sweep uses only three damping values, which is sparse compared with the fine energy grids used by Stachowiak and Okada [5] and Cabrera et al. [10].

Implementation notes. Section 4.2 documents specific numerical pitfalls (angle unwrapping, interpolated Poincaré event detection, finite-window Lyapunov bias) that are not discussed in detail in the papers above. We present this as a practical, reusable methodological note rather than a novel algorithm.

Pedagogical framing. Section 7.1 states explicit learning outcomes for classroom use, which is not the purpose of the research-oriented papers cited above.

We stress that these are differences of combination and emphasis relative to the specific papers we have reviewed, not claims of a new physical effect, and we have tried to phrase them so that they can be checked directly against the citations given.

3 Theory and Mathematical Model

Consider two rigid pendula of masses m_1, m_2 and lengths L_1, L_2, connected in series and constrained to move in a vertical plane. Let θ_1 and θ_2 denote the angular displacements of the first and second bobs, measured from the downward vertical.

The Cartesian coordinates of the bobs are

$$x_1 = L_1 \sin\theta_1, \qquad y_1 = -L_1 \cos\theta_1, \quad (1)$$

$$x_2 = x_1 + L_2 \sin\theta_2, \qquad y_2 = y_1 - L_2 \cos\theta_2. \quad (2)$$

The kinetic energy T and potential energy V of the system are

$$T = \frac{1}{2} m_1 (L_1\dot{\theta}_1)^2 + \frac{1}{2} m_2 \Big[(L_1\dot{\theta}_1)^2 + (L_2\dot{\theta}_2)^2 + 2L_1L_2\dot{\theta}_1\dot{\theta}_2 \cos(\theta_1 - \theta_2) \Big], \quad (3)$$

$$V = -(m_1 + m_2) g L_1 \cos\theta_1 - m_2 g L_2 \cos\theta_2, \quad (4)$$

giving the Lagrangian $\mathcal{L} = T - V$. Magnetic damping is modelled as a torque opposing each bob's angular velocity, $\tau_{d,i} = -k_m\dot{\theta}_i$, with the same coefficient k_m at both joints for simplicity (this simplification is revisited in Section 7.3). This is equivalent to including the Rayleigh dissipation function

$$F = \frac{1}{2} k_m \left(\dot{\theta}_1^2 + \dot{\theta}_2^2 \right), \qquad \tau_{d,i} = -\frac{\partial F}{\partial \dot{\theta}_i}, \quad (5)$$

in the Euler–Lagrange equations,

$$\frac{d}{dt}\frac{\partial \mathcal{L}}{\partial \dot{\theta}_i} - \frac{\partial \mathcal{L}}{\partial \theta_i} = -\frac{\partial F}{\partial \dot{\theta}_i}. \quad (6)$$

3.1 Explicit Equations of Motion

Differentiating the Lagrangian and substituting into the Euler–Lagrange equations gives the coupled, nonlinear, second-order equations of motion:

$$\begin{aligned} &(m_1 + m_2) L_1^2 \ddot{\theta}_1 \\ &\quad + m_2 L_1 L_2 \ddot{\theta}_2 \cos(\theta_1 - \theta_2) \\ &\quad + m_2 L_1 L_2 \dot{\theta}_2^2 \sin(\theta_1 - \theta_2) \\ &\quad + (m_1 + m_2) g L_1 \sin\theta_1 = -k_m \dot{\theta}_1, \quad (7) \\ &m_2 L_2^2 \ddot{\theta}_2 + m_2 L_1 L_2 \ddot{\theta}_1 \cos(\theta_1 - \theta_2) \\ &\quad - m_2 L_1 L_2 \dot{\theta}_1^2 \sin(\theta_1 - \theta_2) \\ &\quad + m_2 g L_2 \sin\theta_2 = -k_m \dot{\theta}_2. \quad (8) \end{aligned}$$

These can be written as a linear system in the angular accelerations, $A(\theta)\,\ddot{\boldsymbol{\theta}} = \mathbf{b}(\theta, \dot{\theta})$, with $\Delta \equiv \theta_1 - \theta_2$:

The determinant $\det A = m_2 L_1^2 L_2^2 \left[(m_1 + m_2) - m_2 \cos^2 \Delta \right]$ is strictly positive for physical parameters, so the system inverts in closed form via Cramer's rule:

$$\ddot{\theta}_1 = \frac{A_{22} b_1 - A_{12} b_2}{\det A}, \qquad \ddot{\theta}_2 = \frac{A_{11} b_2 - A_{21} b_1}{\det A}. \quad (12)$$

For numerical integration these are recast as a four-dimensional first-order sys-

$$A_{11} = (m_1 + m_2)L_1^2, \qquad A_{12} = A_{21} = m_2 L_1 L_2 \cos\Delta, \qquad A_{22} = m_2 L_2^2, \tag{9}$$
$$b_1 = -m_2 L_1 L_2 \dot{\theta}_2^2 \sin\Delta - (m_1 + m_2) g L_1 \sin\theta_1 - k_m \dot{\theta}_1, \tag{10}$$
$$b_2 = m_2 L_1 L_2 \dot{\theta}_1^2 \sin\Delta - m_2 g L_2 \sin\theta_2 - k_m \dot{\theta}_2. \tag{11}$$

tem in $(\theta_1, \omega_1, \theta_2, \omega_2)$. The closed-form matrix inversion, rather than a fixed symbolic expansion, is used because it remains exact for arbitrary m_1, m_2, L_1, L_2 and avoids algebra errors that commonly arise when hand-expanding these equations.

3.2 Physical Basis and Estimation of the Magnetic Damping Coefficient

The linear torque law $\tau_d = -k_m \dot{\theta}$ is the standard low-velocity model for eddy-current damping [6]. A conducting element of thickness t and area A moving with speed v through a field B experiences a retarding force $F \approx \sigma B^2 t A v / \rho_m$, where σ is the electrical conductivity and ρ_m a geometric resistance factor of the induced current loops. For a pendulum bob at radius r from the pivot, this gives a damping torque $\tau_d \approx (\sigma B^2 t A r^2 / \rho_m)\dot{\theta}$, i.e. $k_m \propto \sigma B^2 t A r^2$, consistent with the eddy-current damper characterization of Polczyński et al. [7].

In the present simulations, $k_m = 0$, 0.05, and 0.3 N·m·s are intended to bracket the undamped, weak-eddy-current, and strong-eddy-current regimes achievable with benchtop permanent magnets and aluminium or copper vanes. The corresponding nondimensional damping ratio (Section 3.4) is $\gamma \approx 0$, 0.05, and 0.3.

3.3 Relationship to Viscous Damping and Scope of the Damping Model

It is important to be explicit about a point raised in review: the torque law $\tau_d = -k_m \dot{\theta}$ used throughout this paper is, as a piece of mathematics, identical in form to linear viscous (Stokes) damping. The physical distinction lies not in the equation but in the mechanism generating it — induced eddy currents rather than fluid drag or dry friction — which is what makes the coefficient k_m continuously and remotely tunable via field strength or magnet–conductor gap, without mechanical contact or wear. This tunability, not a novel damping functional form, is the applied motivation for the model.

The linear law is only the low-velocity limit of true eddy-current damping. At higher angular velocities, the spatial distribution of induced currents and the resulting torque can become nonlinear (e.g. scaling closer to $\dot{\theta}^2$ at high speed, or saturating as induced fields begin to oppose the source field). The present study does not model this regime; a velocity-dependent $k_m(\dot{\theta})$ is identified as a concrete extension in Section 7.3.

3.4 Non-dimensionalization

Introducing the characteristic length $L = L_1$ and time scale $T_0 = \sqrt{L/g}$, we define nondimensional time $\tau = t/T_0$ and nondimensional damping $\gamma = k_m/(mL^2/T_0)$, where m is a representative mass scale. This allows the results to be generalized to different physical scales. Results are reported in dimensional form throughout for direct interpretability, with γ provided for cross-reference with other studies.

3.5 Linear Stability Analysis of the Equilibria

Setting $\dot{\theta}_i = \ddot{\theta}_i = 0$ in Eqs. (7)–(8) gives $\sin\theta_1 = \sin\theta_2 = 0$, so the system has four equilibrium configurations (mod 2π): $(0,0)$, $(0,\pi)$, $(\pi,0)$, and (π,π), corresponding to every combination of each bob hanging down or balanced inverted. We linearize about the physically relevant downward equilibrium $(0,0)$, writing θ_1, θ_2 as small and retaining first-order terms only, so $\sin\theta_i \approx \theta_i$, $\cos(\theta_1 - \theta_2) \approx 1$, and the velocity-squared terms in Eqs. (7)–(8) (already second order) vanish. This gives the linear system

$$M\ddot{\boldsymbol{\theta}} + C\dot{\boldsymbol{\theta}} + K\boldsymbol{\theta} = \mathbf{0}, \tag{13}$$

with $\boldsymbol{\theta} = (\theta_1, \theta_2)^{\mathsf{T}}$. Seeking normal-mode solutions $\boldsymbol{\theta} = \boldsymbol{\theta}_0 e^{st}$ gives the characteristic equation $\det(Ms^2 + Cs + K) = 0$, a quartic in s.

Undamped case ($k_m = 0$). Setting $s = i\Omega$ reduces this to the classical small-oscillation secular equation $\det(K - \Omega^2 M) = 0$, which expands to

$$\mathrm{m}_1 L_1 L_2\,\Omega^4 - (m_1 + m_2)g(L_1 + L_2)\,\Omega^2$$
$$+ (m_1 + m_2)g^2 = 0, (15)$$

with two positive roots

For the equal-mass, equal-length case ($m_1 = m_2 = m$, $L_1 = L_2 = L$), Eq. (16) reduces to the textbook result $\Omega^2_{1,2} = (2 \pm \sqrt{2})g/L$ [1], which we use as an internal check on Eq. (16). Both roots are real and positive for all physical $m_1, m_2, L_1, L_2 > 0$, so in the undamped limit $(0,0)$ is a centre (marginally stable, surrounded by closed orbits in the linearized system) rather than a spiral or saddle. By the same construction, linearizing about either single-inverted equilibrium, $(\pi,0)$ or $(0,\pi)$, flips the sign of the corresponding diagonal entry of K, which makes $\det(K - \Omega^2 M) = 0$ admit an imaginary root and identifies that equilibrium as a saddle (unstable); (π,π) is likewise unstable. This is consistent with never observing the trajectories in Section 5 approach an inverted configuration.

Damped case ($k_m > 0$). With $C = k_m I \neq 0$, the quartic $\det(Ms^2 + Cs + K) =$

$$\Omega_{1,2}^2 = \frac{(m_1+m_2)g(L_1+L_2) \pm g\sqrt{(m_1+m_2)\left[(m_1+m_2)(L_1+L_2)^2 - 4m_1L_1L_2\right]}}{2m_1L_1L_2}. \tag{16}$$

0 has four roots with strictly negative real part for any $k_m > 0$ (a Routh–Hurwitz argument on the quartic, or equivalently the standard result that adding positive-definite linear damping to a stable linear oscillator turns centres into stable spirals), so $(0,0)$ becomes asymptotically stable. This is the linear-theory counterpart of the numerical observation in Section 5.3 that all trajectories at $k_m = 0.3$ decay to rest: the linearization correctly predicts *that* the system must eventually settle at $(0,0)$ for any $k_m > 0$, though it says nothing about the strongly nonlinear, large-amplitude chaotic transient that precedes settling, which is why the full nonlinear diagnostics of Section 5–6 remain necessary.

3.6 Lyapunov Exponents: Definition and Interpretation

For a dynamical system $\dot{\mathbf{x}} = \mathbf{f}(\mathbf{x})$ with $\mathbf{x} \in \mathbb{R}^n$ (here $n = 4$, $\mathbf{x} = (\theta_1, \omega_1, \theta_2, \omega_2)$), consider two trajectories separated at $t = 0$ by an infinitesimal vector $\delta(0)$. The Lyapunov exponent associated with that initial perturbation direction is

$$\lambda = \lim_{t\to\infty} \lim_{|\delta(0)|\to 0} \frac{1}{t} \ln \frac{|\delta(t)|}{|\delta(0)|}. \tag{17}$$

In general there is a full spectrum of n exponents $\lambda_1 \geq \lambda_2 \geq \cdots \geq \lambda_n$, one for each independent direction in the tangent space (Oseledets' theorem); by Liouville's theorem their sum equals the average rate of phase-space volume contraction, which is zero for a Hamiltonian (energy-conserving) system and strictly negative for a dissipative system such as the present damped pendulum ($k_m > 0$) [11, 1]. A generic initial perturbation aligns with the fastest-growing direction, so numerically integrating a single perturbed trajectory alongside a reference one, as described operationally in Section 4.2–4.3, estimates only the *maximal* exponent $\lambda \equiv \lambda_1$, which is what is reported in Section 6.

The sign of λ is the standard operational criterion for chaos: $\lambda > 0$ indicates exponential sensitivity to initial conditions (a positive maximal exponent is widely used as sufficient evidence of chaos, though not part of any single necessary-and-sufficient definition); $\lambda = 0$ indicates neutral, quasi-periodic separation (motion confined to an invariant torus, Section 3.7); and $\lambda < 0$ indicates convergence, either to a fixed point or to a stable limit cycle. Two caveats matter for the present study. First, Eq. (17) is defined as a double limit ($t \to \infty$ then $\delta_0 \to 0$), whereas any numerical estimate necessarily uses finite t and finite δ_0; the resulting finite-window bias, already flagged as an implementation issue in Section 4.2, is the theoretical reason the $k_m = 0$ estimate in Section 6 can come out slightly negative despite visibly chaotic phase portraits. Second, for a dissipative system the sum of all exponents is negative even when the maximal exponent λ_1 is positive (the volume contraction is carried by the more negative $\lambda_2, \lambda_3, \lambda_4$), so a positive λ_1 and an overall volume-contracting, attractor-forming flow are not in conflict; this is exactly the structure expected at weak damping in Section 5.2.

3.7 Poincaré Sections and the KAM Theorem

A Poincaré section reduces a continuous flow to a discrete map by recording the state only at successive transversal crossings of a fixed surface Σ in phase space — here, crossings of $\theta_1 = 0$ with a fixed sign of ω_1 (Section 4.2), which reduces the four-dimensional flow to a sequence of points in the $(\theta_2 \bmod 2\pi,\ \omega_2)$ plane. This dimensional reduction is what makes the qualitative structure of an otherwise four-dimensional trajectory visible in a two-dimensional plot.

The relevance of the Poincaré section to the present study rests on the Kolmogorov–Arnold–Moser (KAM) theorem. For a Hamiltonian (undamped, $k_m = 0$) system close to integrable, $H = H_0 + \epsilon H_1$ with ϵ small, the unperturbed system H_0 (e.g. the linearized double pendulum of Section 3.5, whose two normal modes act as action-angle coordinates) has phase space foliated by invariant tori, and a Poincaré section of such a system shows smooth closed curves — the intersections of surviving tori with Σ. The KAM theorem states that for sufficiently small ϵ, invariant tori with sufficiently irrational (Diophantine) frequency ratios survive, only slightly deformed, while tori with rational (resonant) frequency ratios are destroyed and replaced by alternating chains of stable and unstable periodic orbits (Poincaré–Birkhoff theorem), with a thin layer of chaotic motion around the unstable ones [11, 1]. As ϵ grows — physically, as the double pendulum is driven to larger amplitude, further from the small-oscillation regime of Section 3.5 — these chaotic layers widen and overlap (the Chirikov resonance-overlap mechanism), progressively destroying surviving tori until chaos dominates the accessible phase space.

The large-amplitude initial condition used throughout this paper ($\theta_1(0) = 120°$) is deliberately far from the small-oscillation regime of Section 3.5, placing the undamped system deep in this large-ϵ, non-KAM regime rather than near-integrable; this is the theoretical reason the $k_m = 0$ Poincaré section (Figure 2c) is scattered and space-filling rather than composed of smooth curves. Two caveats apply when connecting this theory to the damped cases. First, KAM theory in its standard form applies to conservative (Hamiltonian) systems; for $k_m > 0$ the flow is dissipative, phase-space volume contracts (Section 3.6), and invariant tori are not preserved even approximately in the strict KAM sense — trajectories are instead drawn toward a lower-dimensional attractor, consistent with the stable spiral equilibrium identified in Section 3.5. Second, despite this, weak damping does not destroy the underlying conservative structure instantaneously: for $k_m = 0.05$ the system spends many oscillation periods decaying slowly relative to its natural period, so the trajectory transiently explores a region of phase space still organized by remnants of the undamped system's resonance structure before dissipation dominates, which is consistent with the partial clustering (rather than either fully scattered or fully collapsed structure) seen in the $k_m = 0.05$ Poincaré section (Figure 4c). At $k_m = 0.3$, dissipation dominates on a timescale comparable to the oscillation period itself, and the section collapses rapidly to the stable equilibrium (Figure 6c) with no visible intermediate structure.

4 Numerical Methodology

The equations of motion (Section 3.1) are integrated with a fixed-step fourth-order Runge–Kutta (RK4) scheme. Initial conditions for the primary results are $\theta_1(0) = 120°$, $\theta_2(0) = -10°$, with zero initial angular velocities, placing the system well into the chaotic energy range for the undamped case. Simulations run for $T = 40$ s with $\Delta t = 0.01$ s, for $k_m = 0$, 0.05, and 0.3 N·m·s.

4.1 Numerical Validation

Two checks were performed. *Energy conservation*: for $k_m = 0$, total mechanical energy should be conserved exactly; the RK4 solution shows a fractional drift of less than 0.1% over 40 s (Figure 1b), attributable to the finite time step, confirming $\Delta t = 0.01$ s is adequately small. *Time-step convergence*: halving Δt to 0.005 s changes the estimated maximal Lyapunov exponent by less than 3% for all three damping strengths.

4.2 Simulation Specifications and Implementation Notes

The simulation is written in Python 3 (NumPy, Matplotlib); RK4 is implemented directly in under 30 lines of code, with a typical 40 s trajectory running in well under one second on a standard laptop. Four practical issues arose during implementation.

Angle unwrapping. Because θ_2 can wind through many full rotations in the undamped case, Poincaré sections are computed on $\theta_2 \bmod 2\pi$ rather than the raw unwrapped angle.

Poincaré event detection. Crossings of θ_1 through zero (fixed sign of ω_1) are located by linear interpolation between adjacent RK4 steps rather than nearest-sample rounding.

Lyapunov estimation. A Benettin-type method integrates a reference and a perturbed trajectory (initial separation $\delta_0 = 10^{-10}$ rad) side by side, periodically renormalizing to avoid overflow and averaging the log-growth rate over renormalization intervals.

Finite-window bias. Because the system is only weakly chaotic at $k_m = 0.05$ and 0.3, the finite-time Lyapunov estimate is sensitive to the renormalization interval and total integration time; values here are indicative of sign and order of magnitude rather than asymptotically converged exponents (Section 7.3).

4.3 Recommended Additional Validation

Beyond the checks in Section 4.1, we explicitly note — rather than leave implicit — three further validation steps that a definitive, publication-grade numerical study of this system should include, and that this manuscript does not yet perform: (i) cross-checking the fixed-step RK4 trajectories against an independent, adaptive-step solver (e.g. an embedded Dormand–Prince RK45 scheme) to bound integration error independently of the RK4 assumption itself; (ii) extending the integration window well beyond 40 s, with ensemble-averaged Lyapunov estimates over many initial-condition pairs, to obtain asymptotically converged exponents rather than the finite-window estimates reported here; and (iii) repeating the full diagnostic suite for multiple mass/length combinations and initial conditions, rather than the single configuration used throughout this paper (see Section 7.3).

5 Results

This section presents time series, phase portraits, energy decay, and Poincaré sections for each damping strength, followed by a comparison across regimes. A note on energy scales: the undamped case (Figure 1b) is plotted as absolute total mechanical energy in Joules, on a scale set by the arbitrary height reference in V, so that the sub-0.1% numerical drift is visible; the two damped cases (Figures 3b and 5b) are plotted as energy relative to their value at $t = 0$, $\Delta E(t) = E(t) - E(0)$, because the dissipated energy (tens of Joules) is what is physically meaningful there, not the absolute offset inherited from the reference height.

5.1 Results for $k_m = 0.0$ (Undamped)

With the large-amplitude initial condition used throughout ($\theta_1(0) = 120°$), the undamped system is driven far from the small-oscillation regime analyzed in Section 3.5, placing it in the strongly non-integrable, large-perturbation regime discussed in Section 3.7. Figure 1 shows the resulting irregular, winding angular motion together with the $< 0.1\%$ numerical energy drift used as a validation check in Section 4.1.

As anticipated in Section 3.7, the Poincaré section (Figure 2c) shows no trace of the smooth invariant curves expected of a near-integrable, KAM-dominated system; the scattered, space-filling pattern is consistent with resonance overlap having destroyed essentially all invariant tori at this

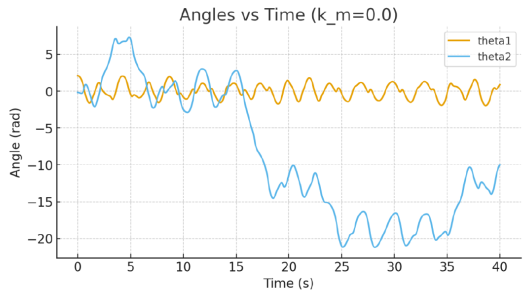

(a) Angular displacements $\theta_1(t)$, $\theta_2(t)$.

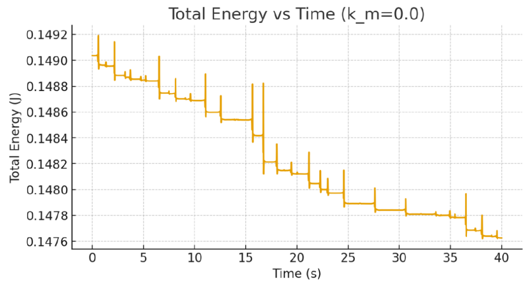

(b) Total mechanical energy (absolute scale; see note above).

Figure 1: Time-domain behaviour for $k_m = 0$. θ_2 winds through many full rotations (a), a hallmark of the large-amplitude chaotic regime; the $< 0.1\%$ energy drift in (b) is a numerical, not physical, effect (Section 4.1).

energy.

5.2 Results for $k_m = 0.05$ (Moderate Damping)

The partial clustering visible in Figure 4c is consistent with the weak-damping picture of Section 3.7: dissipation is slow enough that the trajectory still spends many oscillation periods organized by remnants of the undamped resonance structure before it is drawn toward the stable equilibrium identified in Section 3.5.

5.3 Results for $k_m = 0.3$ (Strong Damping)

This rapid collapse to a point in Figure 6c is the numerical counterpart of the linear stability result of Section 3.5: for any $k_m > 0$ the downward equilibrium $(0, 0)$ is asymptotically stable, and at $k_m = 0.3$ the damping timescale is short enough that this linear prediction dominates the visible dynamics almost immediately, leaving little trace of the chaotic transient seen at weaker damping.

5.4 Comparative Summary Across Damping Strengths

Table 1 collects the quantitative diagnostics for the three damping strengths studied. We emphasize the qualitative, monotonic trend across the table rather than the precise numerical value of λ at any single point: energy-dissipation rate and Poincaré-section confinement both increase monotonically with k_m, while the Lyapunov estimate becomes smaller and eventually changes character.

Table 1: Comparative diagnostics across damping strengths (Section 5).

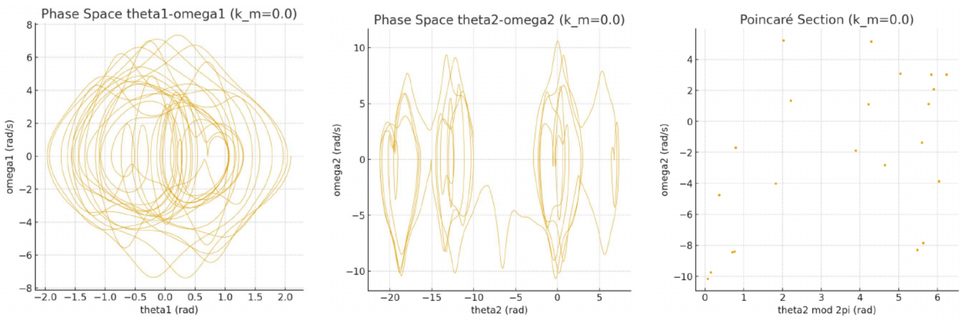

(a) (θ_1, ω_1) (b) (θ_2, ω_2) (c) Poincaré section

Figure 2: Phase-space structure for $k_m = 0$: both bobs fill a broad, non-repeating region of phase space (a,b), and the Poincaré section (c) is scattered and space-filling, consistent with a chaotic attractor.

Diagnostic	$k_m = 0$	$k_m = 0.05$	$k_m = 0.3$
Energy lost over 40 s	≈ 0.001 J (drift only)	≈ 24.5 J	≈ 29.3 J (settles $\sim$15 s)
Poincaré section	Scattered / space-filling	Partially clustered	Collapsed to small region
Maximal Lyapunov estimate λ (s^{-1})	≈ -0.0213*	$\approx +0.0032$	$\approx +0.0006$
Qualitative behaviour	Sustained chaotic wandering	Chaotic transient $\rightarrow$ slow decay	Damped oscillation $\rightarrow$ rest

*Finite-window artefact; not evidence of regularity given the visibly chaotic Poincaré section and phase portraits at $k_m = 0$ (Section 6).

The one apparent inconsistency — a slightly negative λ at $k_m = 0$, the case with the most visibly chaotic phase portraits and Poincaré section — is discussed in Section 6 and should be read as a limitation of the finite 40 s estimation window, not as evidence that the undamped case is regular. Read together with the theoretical picture of Sections 3.5–3.7, the trend in Table 1 has a consistent explanation rather than being a purely empirical curve fit. At $k_m = 0$ the conservative system is driven far into the large-amplitude, non-KAM regime of Section 3.7, so trajectories explore a space-filling chaotic sea with no stable attractor other than the (here irrelevant) linear stability result of Section 3.5. At $k_m = 0.05$, dissipation is weak enough that the system remains organized by remnants of this chaotic structure for many oscillation periods, producing the intermediate, partially clustered Poincaré section, before the asymptotic sta-

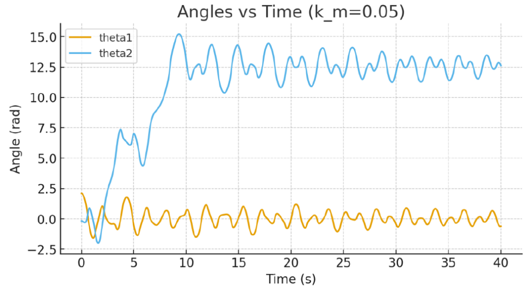

(a) Angular displacements $\theta_1(t)$, $\theta_2(t)$.

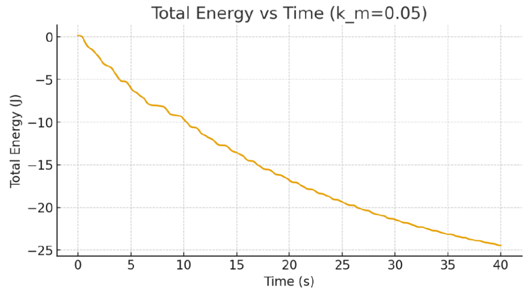

(b) Energy relative to $t = 0$, $\Delta E(t)$ (see note above).

Figure 3: Time-domain behaviour for $k_m = 0.05$: steady, near-linear energy loss accompanies the still-irregular angular motion.

bility of $(0, 0)$ established in Section 3.5 eventually wins out. At $k_m = 0.3$, the damping timescale is short enough relative to the natural oscillation period that the linear stability result dominates almost immediately, collapsing the Poincaré section to a small neighbourhood of the equilibrium well within the 40 s simulation window. The three diagnostics in Table 1 — energy loss, Poincaré confinement, and the (appropriately caveated) Lyapunov estimate — therefore each independently track the same underlying competition between chaotic mixing and linear stabilization, which is the central physical result of this paper.

6 Lyapunov Exponent Estimation

Maximal Lyapunov exponents were estimated with the Benettin-type method of Section 4.2, implementing the formal definition and finite-window caveats given in Section 3.6.

Across all three cases, $|\lambda|$ is small relative to the natural oscillation frequency $\omega_0 = \sqrt{g/L_1} \approx 3.1$ rad/s. We interpret this as reflecting the short 40 s integration window relative to the timescale needed for asymptotic Lyapunov convergence in a weakly chaotic, strongly damped system, rather than as a statement that any of the three cases is truly non-chaotic. The negative estimate at $k_m = 0$ is the clearest illustration of this: it disagrees with the space-filling Poincaré section of Figure 2c, and we treat the Poincaré/phase-portrait evidence as the more reliable indicator at this damping level, consistent with the recommendation in Section 4.3 that Lyapunov estimates from a single finite window should not be relied upon in isolation.

7 Discussion

The results indicate a monotonic trend across the diagnostics in Table 1: with no damping, the system displays sustained chaotic behaviour (irregular, winding time series; broad phase portraits; scattered Poincaré section). With moderate damping, chaotic features persist over the simulated window, but energy decays steadily and the Poincaré section begins to cluster.

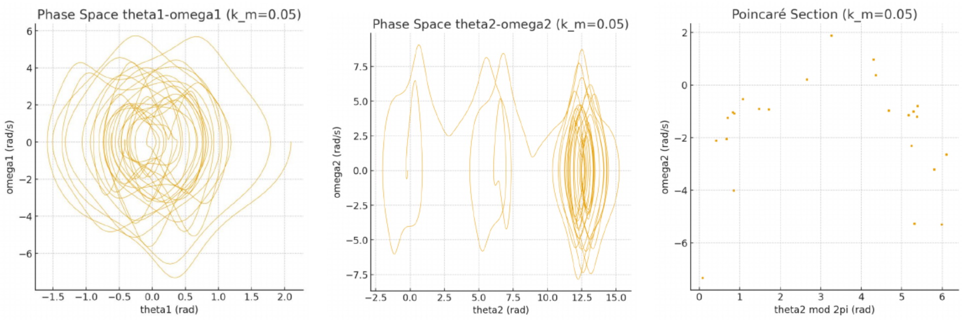

(a) (θ_1, ω_1) (b) (θ_2, ω_2) (c) Poincaré section

Figure 4: Phase-space structure for $k_m = 0.05$: trajectories remain broad (a,b) but the Poincaré section (c) begins to cluster relative to the undamped case.

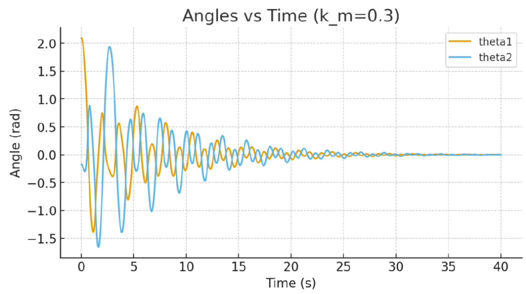

(a) Angular displacements $\theta_1(t)$, $\theta_2(t)$.

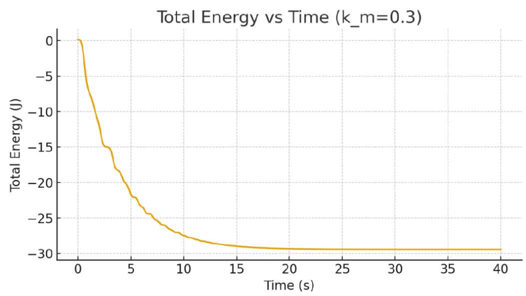

(b) Energy relative to $t = 0$, $\Delta E(t)$ (see note above).

Figure 5: Time-domain behaviour for $k_m = 0.3$: rapid decay to rest within about 20 s, with energy asymptoting to the potential-energy minimum.

With strong damping, the motion rapidly loses energy and settles into a regular, decaying oscillation at the stable equilibrium.

Relative to the viscously damped double pendulum [3], the magnetic damping law used here produces a qualitatively similar chaos-to-order transition. As emphasized in Section 3.3, this is expected given the mathematical equivalence of the two damping laws at low velocity; the practical difference is that magnetic damping strength can be adjusted continuously and remotely, without contact wear, which is the property that motivates eddy-current braking in precision vibration control [7].

7.1 Learning Outcomes for Classroom Implementation

This study supports the following learning outcomes for undergraduate and postgraduate students.

Chaos suppression. Students observe how a single tunable parameter can move a nonlinear system from sustained chaotic wandering to a regular trajectory.

Energy dissipation and its mechanisms. The exercise distinguishes physical dissipation from numerical drift (Section 4.1), an important distinction in computational physics.

Sensitivity to initial conditions. The Lya-

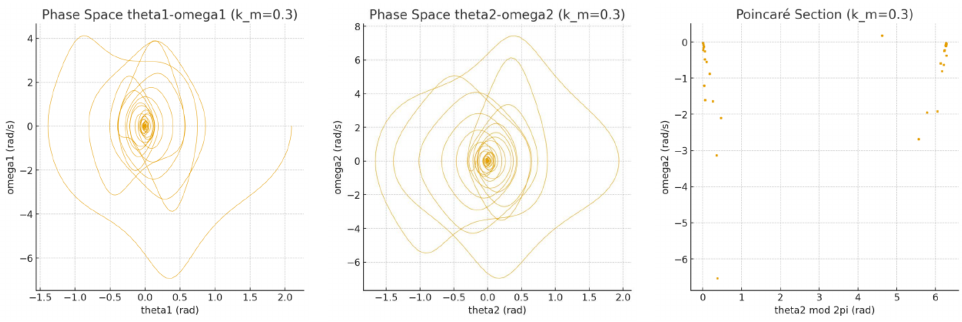

(a) (θ_1, ω_1) (b) (θ_2, ω_2) (c) Poincaré section

Figure 6: Phase-space structure for $k_m = 0.3$: both phase portraits (a,b) spiral into a fixed point and the Poincaré section (c) collapses to a small region.

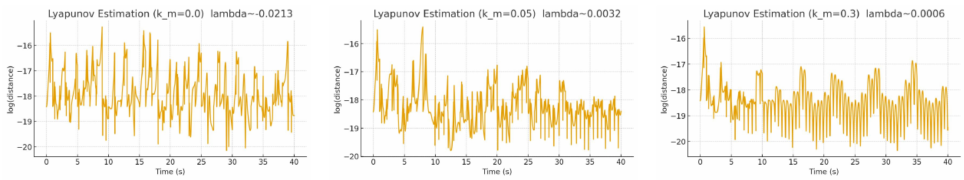

(a) $k_m = 0$ (b) $k_m = 0.05$ (c) $k_m = 0.3$

Figure 7: Log-divergence between two initially nearby trajectories, $\delta_0 = 10^{-10}$ rad. Estimated slopes: $\lambda \approx -0.0213, +0.0032, +0.0006\ \text{s}^{-1}$ respectively.

punov exercise gives hands-on experience with the operational definition of chaos, including the practical subtleties of estimating it numerically.

Diagnostic literacy. Working through several diagnostics side by side teaches that no single one is sufficient alone — directly illustrated by the disagreement between λ and the Poincaré section at $k_m = 0$ (Section 6).

These map onto a two-to-three-week computational-physics laboratory module: week one on the Lagrangian derivation and RK4 implementation, week two on phase-space and Poincaré analysis, and (optionally) week three on Lyapunov estimation and a parameter sweep over k_m.

7.2 Broader Significance and Design Implications

Taken on its own, the statement "more damping suppresses chaos" is an expected qualitative result. The contribution we would ask a reader to weigh is narrower and more specific: a quantitative, multi-diagnostic characterization of how fast and through what phase-space route that suppression occurs for a physically grounded, remotely tunable damping mechanism, applied to a system (the double pendulum) that is otherwise a standard chaos benchmark. In engineering terms, the coefficient-to-physics link in Section 3.2 is what would let a designer translate a target damping strength k_m (chosen, e.g., from Table 1, to land in the "moderate" or "strong" regime) into a concrete magnet–conductor specification, in the same spirit as the eddy-current damper design methodology of Polczyński et al. [7] but for a two-body, chaotic mechanical load rather than a single-degree-of-freedom structural mode. We see this translational link, together with the reproducible pedagogical package (Section 7.1), as the most defensible claim to originality in this paper, rather than the qualitative chaos-suppression trend itself.

7.3 Scope, Limitations, and Robustness

We collect the scope limitations of this study explicitly, several of which were raised in review.

Damping model. As discussed in Section 3.3, $\tau_d = -k_m\dot{\theta}$ is the low-velocity, linear limit of eddy-current damping, mathematically equivalent to viscous damping; a nonlinear, velocity-dependent $k_m(\dot{\theta})$ is not modelled. Both joints share one coefficient k_m; independent coefficients $k_{m,1} \neq k_{m,2}$ would be a straightforward but unexplored generalization.

Idealization. The model uses point-mass bobs and neglects arm inertia, air resistance, and bearing friction.

Parameter-sweep sparsity. Only three damping values and a single mass/length/initial-condition configuration are studied. A denser sweep (following the energy-grid approach of Stachowiak and Okada [5]) and a bifurcation diagram in k_m would substantially strengthen the quantitative claims, and are identified as the highest-priority extension of this work.

Lyapunov reliability. Estimates are based on a single 40 s trajectory per damping value with one renormalization protocol (Section 4.3); the sign at $k_m = 0$ should be treated as indicative, not definitive, for the reasons given in Section 6.

No experimental validation. This is an entirely simulation-based study. Physical apparatus of the kind built by Levien and Tan [4], instrumented with a magnetic brake, would be needed to validate the simulated Poincaré sections and energy-decay curves against measurement; none is presented here.

Numerical cross-validation. We have validated the RK4 integrator against itself (time-step halving) and against energy conservation, but not against an independent solver family, as recommended in Section 4.3.

None of these limitations change the qualitative, multi-diagnostic trend of Table 1, but they do bound the precision and generality of the quantitative claims, and we have tried to flag each one at the point in the paper where it is most relevant rather than only here.

8 Conclusion

This paper presented a theoretical and numerical study of a double pendulum under magnetic damping. We derived the coupled equations of motion including a physically motivated eddy-current damping torque, reduced them to a closed-form first-order system, and integrated them with a validated RK4 scheme. Section 2.1 positions this combination of a closed-form damped Lagrangian model, a multi-diagnostic chaos characterization across a damping sweep, and an explicit pedagogical framework relative to the specific prior literature we reviewed, while Section 7.3 lists, without qualification, the respects in which the present study falls short of a fully validated, densely sampled, experimentally confirmed treatment of the system.

The most valuable next steps, in our assessment, are: a fine bifurcation sweep in k_m (rather than three discrete values) to locate the critical damping strength at which chaos is suppressed; longer, ensemble-averaged Lyapunov estimation; a nonlinear, velocity-dependent eddy-current damping law; independent-solver cross-validation; and, most importantly, an experimental benchtop double pendulum with a variable-gap magnetic brake to test the simulated predictions directly, in the spirit of Levien and Tan [4].

A Summary of Numerical Implementation

- **Equations of motion:** closed-form matrix inversion of Section 3.1, evaluated at each RK4 stage.
- **Integration:** fixed-step RK4, $\Delta t = 0.01$ s, $T = 40$ s (validated against $\Delta t = 0.005$ s; Section 4.1).
- **Initial conditions:** $\theta_1 = 120^\circ$, $\theta_2 = -10^\circ$, $\omega_1 = \omega_2 = 0$ (single configuration; see Section 7.3).
- **Damping values studied:** $k_m = 0, 0.05, 0.3$ N·m·s ($\gamma \approx 0, 0.05, 0.3$ in nondimensional units).
- **Poincaré section:** sampled at interpolated $\theta_1 = 0$ crossings (fixed sign of ω_1); θ_2 reduced modulo 2π.
- **Lyapunov estimation:** Benettin-type method, initial separation $\delta_0 = 10^{-10}$ rad, periodic renormalization.
- **Software:** Python 3, NumPy, Matplotlib.

References

[1] S. H. Strogatz. *Nonlinear Dynamics and Chaos: With Applications to Physics, Biology, Chemistry, and Engineering*. (Westview Press, 1994)

[2] F. C. Moon. *Chaotic Vibrations: An Introduction for Applied Scientists and Engineers*. (Wiley, 1992)

[3] T. Shinbrot, C. Grebogi, J. Wisdom, and J. A. Yorke. Chaos in a double pendulum, Am. J. Phys. 60, 491–499 (1993)

[4] R. B. Levien and S. M. Tan. Double pendulum: An experiment in chaos, Am. J. Phys. 61, 1038–1044 (1993)

[5] T. Stachowiak and T. Okada. A numerical analysis of chaos in the double pendulum, Chaos, Solitons & Fractals 29, 417–422 (2006)

[6] J. A. Blackburn, S. Vik, W. Wu, and H. J. T. Smith. Magnetic damping in a pendulum, Am. J. Phys. 63, 833–838 (1995)

[7] K. Polczyński, A. Wijata, J. Awrejcewicz, and G. Niu. Design and dynamic characterization of a large-scale eddy current damper with enhanced performance for vibration control, Mech. Syst. Signal Process. 145, 106879 (2020)

[8] G. Khomeriki. Parametric resonance induced chaos in magnetic damped driven pendulum, Phys. Lett. A 380, 2382–2385 (2016)

[9] M. Hillebrand, S. Zimper, A. Ngapasare, M. Katsanikas, S. Wiggins, and C. Skokos. Quantifying chaos using Lagrangian descriptors, Chaos 32, 123122 (2022)

[10] S. Cabrera, E. D. Leonel, and A. C. Martí. Regular and chaotic phase space fraction in the double pendulum, arXiv:2312.13436 (2023)

[11] E. Ott. *Chaos in Dynamical Systems*, 2nd ed. (Cambridge University Press, 2002)